Theoretical investigation of the reactivity of bispentamethylcyclopentadienyl uranium(IV) bisthiolate complexes with the heteroallene molecules CS2 and CO2

Fatiha Talbi, Ludovic Castro, Farida Kias, Aziz Elkechai, Abdou Boucekkine, Michel Ephritikhine

Theoretical Investigation of the Reactivity of Bispentamethylcyclopentadienyl Uranium(IV) Bisthiolate Complexes with the Heteroallene Molecules CS_2 and CO_2

Fatiha Talbi,[†] Ludovic Castro,[‡] Farida Kias,[†] Aziz Elkechai,[†]* Abdou Boucekkine [§]* and Michel Ephritikhine [¶]

[†]*Laboratoire de Physique et Chimie Quantique, Faculté des Sciences, Université Mouloud Mammeri de Tizi-Ouzou, 15000 Tizi-Ouzou, Algeria*

[‡] *Université Grenoble Alpes, CNRS UMR 5819, CEA, SyMMES, 38000 Grenoble, France*

[§]*Univ Rennes, ISCR, UMR 6226 CNRS, Campus de Beaulieu, 35042 Rennes Cedex, France*

[¶] *NIMBE, CEA, CNRS, Université Paris-Saclay, CEA-Saclay, 91191 Gif-sur-Yvette, France*

*** Corresponding Authors:**

E-mail: A.B : abdou.boucekkine@univ-rennes1.fr

A.E: azizelkechai@yahoo.fr

Abstract

The insertion reactions of the bispentamethylcyclopentadienyl bisthiolate uranium(IV) complexes $[U(Cp^*)_2(SR)_2]$ ($Cp^* = \eta$–C_5Me_5; R = Me (**1**), ^{t}Bu (**2**), ^{i}Pr (**3**), Ph (**4**)) with CO_2 or CS_2 were investigated using Density Functional Theory (DFT), solvent effects being taken into account using the SMD continuum solvation model. The optimized geometries of the bisthiolate compounds computed at the DFT/B3PW91 level are in good agreement with available X–ray experimental data. The energy profiles of their reactions with CO_2 and CS_2 were determined. The formation of the products can be explained by a unique reaction mechanism involving an uranium(IV)–bridged heteroallene transition state. The CO_2 insertion reactions exhibit lower activation barriers than those of CS_2 insertion in accordance with the experiments showing that the CO_2 insertion reactions are faster. As expected, compound **2** (R = ^{t}Bu) was found to be the most difficult to undergo the insertion reaction because of steric hindrance. The geometrical parameters of the CS_2 insertion derivative $[U(Cp^*)_2(S^tBu)(S_2CS^tBu)]$ (**5**) and the mixed insertion complex $[U(Cp^*)_2(O_2CS^tBu)(S_2CS^tBu)]$ (**6**) obtained after treatment of **5** with CO_2 are consistent with those determined by X-ray diffraction. The performed orbital analysis reveal the respective role of the actinide 7s, 6d and 5f orbitals, whereas the Wiberg Bond Indices (WBI) afford a good explanation of the structural variations during the insertion reactions. Finally, the Natural Population Analyses account for the different charge transfers occurring during the insertion processes.

Keywords: Bisthiolate Uranium(IV) Complexes. CO_2 and CS_2 activation. Insertion reactions. DFT. Transition state.

1. Introduction

The nuclear waste reprocessing and environmental issues made actinide chemistry a significant field of industrial and academic research. Moreover, the activation of inert small molecules like carbon dioxide CO_2 is an important area invested these last decades by the chemists who are challenged to develop a new chemistry, known as `green–chemistry'. Among investigated issues, the transformation of hydrocarbons, as alkanes, by the means of the activation of the C–H bond, the design of new approaches to store or transform usefully CO_2, the removal of polluting gases such CFCs through C–F bond activation as well as the use of renewable sources of CH_4 in various industrial sectors [1–4].

Considering uranium complexes, the insertion reactions of the U–E bonds (E = C, F, H, N, O, Se) have been extensively studied, in particular for the complexes carrying the ubiquitous cyclopentadienyl ring and its derivatives [5], and this has resulted in a large variety of actinide complexes with interesting structural features, coordination environments, and reactivity **[6–18]**. Thus, in order to understand the mechanistic processes involved in these reactions and the role of different ligands coordinated to the metal center**,** the reactivity of uranium complexes towards CO_2 and CS_2 have been explored theoretically by Ding **[19]** and co–workers, who demonstrated that the functionalization of CO_2 or CS_2 when dealing with the $[U(Tp^*)_2(CH_2Ph)]$ (Tp* = hydrotris(3,5–dimethylpyrazolyl)borate) uranium complex proceeds in a two steps process; the insertion of these small molecules into the U–C bond takes place during the first step and is followed by the reorientation of the $PhCH_2CE_2^-$ (E = O, S) fragment to give the final products. Also, Castro *et al*. treated the reactivity of the uranium(III) compound $[U(MeC_5H_4)_3]$ **[20]** with CS_2, COS, PhN_3 and PhNCO using DFT computations and the B3PW91 functional, and could explain the difference in reactivity between CS_2 and COS, and between PhN_3 and PhNCO. Recently, Cloke *et al* investigated experimentally the reductive activation of CO_2 using the mixed–ligand U(III) compound [U(Cp*)(*p*–Me2bp)] (*p*–Me2bp = $C_6H_4\{p–C(CH_3)_2C_6H_2Me_2O^-\}_2$) **[21]**, exhibiting an η^6 interaction with the uranium center, which gave the dinuclear uranium carbonato complex, $[\{U(Cp^*)(p–Me_2bp)\}_2(\mu–\eta^1:\eta^2–CO_3)]$.

On the contrary, very little attention was devoted to the M–S metal–sulfur bonds; their discovery in 1982, in the active site of the metalloproteinase **[22]** boosted the chemistry of the thiolate and sulfide complexes of transition metals which were appreciated for their uses in bioinorganic chemistry, in the study of the nitrogenases **[23],** and in some industrial processes like oil desulfurization **[24]**. The actinide thiolate complexes have been practically ignored for a long time, certainly because the U–S bond between a hard metal and a soft atom was reputed to

be unstable. Ten years later, this assertion proved to be false with in particular the synthesis and/or the characterization of some thiolate actinide compounds, $[U(HBpz_3)_2(S^iPr)_2]$ (pz = pyrazolyl) **[25]**, $[Th(Cp^*)_2(S^nPr)_2]$ **[26]**, $[Li(dme)]_4[U(SCH_2CH_2S)_4]$ **[27]**, $[U(MeC_5H_4)_3(S^iPr)]$, $[U(Me_3CC_5H_4)_3(SPh]$ and $[U(Me_3CC_5H_4)_2(\mu\text{–}SPh)]_2$ **[28]**, $[U(N(SiMe_3)_2)_3(S\text{–}2,6\text{–}Me_2C_6H_3)]$ **[29]** and more recently $[U(Tp^*)_2X]$ (X= CCPh, $CCSiMe_3$, NHPh, $NHCH_2Ph$, SPh) **[30]**. These syntheses show that uranium exhibits a strong affinity for sulfur. Generally, the studies of these thiolate complexes were limited to structural investigations, like those reported by Ephritikhine *et al*. on the monocyclooctatetraenyl and triscyclopentadienyl complexes $[U(Cot)(SR)_2]$ (Cot = $\eta\text{–}C_8H_8$) **[31a]** and $[U(C_5H_4R')_3(SR)]$ (R'= H, ^{t}Bu, $SiMe_3$) **[31b]**. The first reactivity studies on $[U(Cp)_3(S^iPr)]$ (Cp = $\eta\text{–}C_5H_5$) showed that the thiolate ligand could undergo substitution reactions and that unsaturated molecules could be inserted into the U–S bond **[32]**. In particular, treatment of $[U(Cp)_3(S^iPr)]$ with carbon dioxide led to the formation of $[U(Cp)_3(O_2CS^iPr)]$, the first compound resulting from the insertion of CO_2 into a metal–sulfur bond **[31b]**, even if this complex could not be isolated in a pure form because of the facile reverse decarboxylation reaction. However, concerning the uranium(IV) species, especially the complexes involving U–S bonds, the theoretical study of the CO_2 and CS_2 insertion into these bonds has not been developed and the understanding of the reaction mechanism not yet completely clarified. So, with the aim of probing various aspects of the reactivity of uranium(IV) thiolate complexes towards small molecules as CO_2 and CS_2, we found interesting to investigate theoretically the insertion process of these molecules into the U–S bonds of the bisthiolate compounds $[U(Cp^*)_2(SR)_2]$ **[32]**, which can be considered as models in organouranium chemistry **[33]**.

Here, we present a detailed DFT study of the reactivity of a series of bispentamethylcyclopentadienylbisthiolate uranium(IV) complexes, *i.e.*$[U(Cp^*)_2(SMe)_2]$ (**1**), $[U(Cp^*)_2(S^tBu)_2]$ (**2**), $[U(Cp^*)_2(S^iPr)_2]$(**3**)and $[U(Cp^*)_2(SPh)_2]$ (**4**) (Figure 1) towards small heteroallene molecules. The aim is to compare the insertion reactions of CO_2 and CS_2 into actinide–sulfur bonds and to explain their distinct behavior. Indeed, it was found experimentally that the insertion of CO_2 into the U–S bond of the thiolate complexes is easier and faster than that of CS_2. In particular, we shall investigate what are the electronic and steric factors of the SR thiolate ligands which drive this insertion reactivity of the U(IV) complexes under consideration. The reaction profiles of the reaction will be determined. Moreover, to yield further insight into the interactions between uranium and small molecules, key features of the electronic and geometric structures will be explored; in particular Wiberg Bond Indices (WBI) **[34]** and the Natural Population Analysis (NPA) **[35]** will be used to characterize the bonding and electronic structure of the considered species, during the reaction paths.

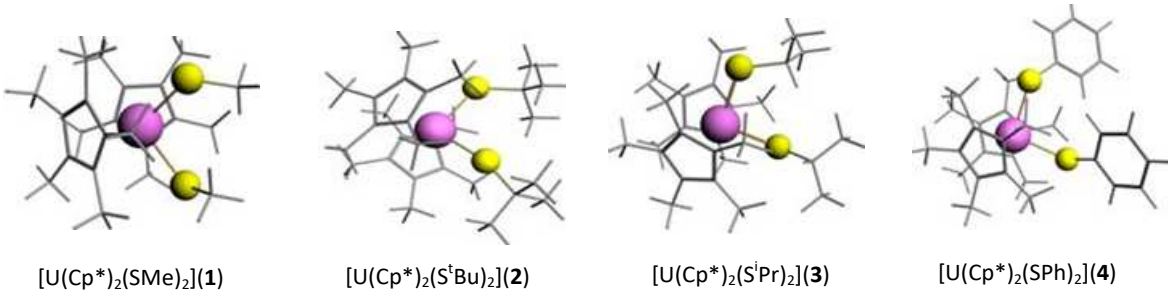

Figure 1. Studied bisthiolate uranium(IV) complexes.

2. Computational details

Calculations were performed with the Gaussian 09 suite of programs [36]. Density Functional Theory (DFT) was applied by the mean of the B3PW91 hybrid functional [37, 38]. In order to treat the actinide center in a suitable way and to greatly reduce computational cost of calculations, two possible relativistic RECP pseudopotentials can be used: the first one where 5f electrons are included in the large–core RECP, and the second one, when active 5f electrons must be described explicitly, being the small–core RECP. According to these considerations, Castro *et al*. developed two kinds of potentials in relativistic effective core to describe suitably the metal actinide: i.e. small–core Stuttgart–Dresden RECP [39] (which includes 1s, 2s, 2p, 3s, 3p, and 3d electrons) and large–core Stuttgart–Dresden RECP [40] (which includes in addition, 4s, 4p, 4d, and 4f electrons) depending on the size of the system.
In the case of actinide U(IV) complexes it has been shown that the large-core RECPs can be used for uranium instead of small-core ones with no less of accuracy (and a shorter computational time) [39]. The RECPs were used in combination with their optimized valence basis sets supplemented by an f polarization function for the large–core RECP used for uranium. The small–core Stuttgart–Dresden relativistic effective core potential [41] was employed for sulfur atoms in association with its valence basis set and an additional d–polarization function [42], while the 6–31+G(d, p) double zeta basis set was used for the treatment of carbon, oxygen and hydrogen atoms [43]. All geometry optimizations were first carried out without any symmetry constraint considering the whole molecular systems in the gas–phase. The solvent effects have been taken into account by a self-consistent reaction field technique using the Solvation Model Density (SMD) continuum model [44] which considers the charge density of the solute interacting with the solvent considered as a dielectric medium.

The solvents considered in our computations are those used in the experimental work of Ephritikhine and al. [5], i.e. tetrahydrofuran (THF) and toluene.

Several studies have shown that the B3PW91 approach reproduces the experimental geometries and ground state properties of f–element compounds with a satisfying accuracy [45-50] in other words, that the theoretical results are found close to those determined experimentally.

All obtained stationary points located on the PES were characterized as extrema which could be minima (adducts, intermediate states with a number of imaginary frequencies Nimag = 0) or first order transition states (Nimag = 1) through harmonic approximation vibration frequency calculations. The zero–point vibrational energy (ZPVE) corrections within the harmonic approximation were calculated and included in all reported relative energies given in kcal.mol^{-1}, obtained for a temperature of 298.15 K. The Intrinsic Reaction Coordinate (IRC) method [51] was used to confirm the transition states linking the two corresponding minima (adducts, intermediates states or final products). In order to simulate the effects of solvent used in the insertion reactions, we carried out "single–point" calculations with the SMD continuum solvation model [52] implemented in Gaussian 09 software.

Spin–orbit corrections to the energies of the reactants and all other states, *i.e.* adducts, transition states, products, have not been considered, since their effects should be similar for all species during the reaction processes reminding that the latter do not involve any change in the oxidation state of the metal, and therefore will not affect the reaction profile. Indeed, these corrections, mainly of atomic nature [53, 54] namely not very sensitive to the environment of the metal ion for a given oxidation state, have a little effect on the computed geometries of actinide molecular compounds and on chemical reactions energies differences [55, 56]. It should be noted that in our case, spin contamination, which can occur in DFT calculations since the used unrestricted determinant could exhibit an unwanted mixing of different spin states, was found negligible, owing to the fact that the computed values $\langle S^2 \rangle$ of the squared spin operator are very close to the exact S(S+1) values for all the studied species (deviation less than 1%).

The bonding in molecules is often described using the classical chemical ideas of covalency (bond multiplicity) and ionicity (atomic charges). The Wiberg bond order is a measure of electron population overlap between two atoms; using orthonormalized basis functions, it is not calculated the same way as in the Mulliken population analysis (MPA) [57]. For typical chemical bonds, usefully the Wiberg bond order value is generally close to the formal bond

order. Besides, the charges derived from the Natural population analysis (NPA) are also more chemically meaningful than MPA charges because they are less basis-set dependent.

3. Results and discussion

3.1. Structural Properties

First, the full geometry optimizations of the neutral complexes, $[UCp^*_2(SMe)_2]$(**1**), $[UCp^*_2(S^tBu)_2]$(**2**) , $[UCp^*_2(S^iPr)_2]$(**3**) and $[UCp^*_2(SPh)_2]$(**4**), were carried out in the gas phase, at the unrestricted DFT level of theory using both the hybrid functionals B3PW91 and B3LYP. For all the U(IV) $5f^2$ complexes, we considered the lowest spin state, i.e. the singlet one which, according to our calculation, corresponds to the ground state. In Table 1 are listed the most relevant computed geometrical parameters, *i.e.* metal–ligand lengths and bond angles for the studied complexes in the gas phase, and in solution for complex **1** at the DFT/B3PW91 level (the optimized structures and coordinates are given in Supporting Information). Our discussion will be focused first on the optimized geometries obtained for the isolated molecules. As expected, in all the studied molecules, the uranium center is found in a classical pseudo–tetrahedral bent sandwich configuration. The computed U–S bond lengths of all thiolate complexes vary from 2.69 to 2.75 Å and are similar to those observed in other neutral thiolate compounds.

Table 1. Selected Bond Lengths (Å) and Angles (deg) for Compounds 1–4 Computed at the B3PW91 and B3LYP (in parentheses) Levels in the Gas Phase (in Solution, Solely for the Complex 1 in THF with B3PW91 Functional, in Red Color; X-ray Values in Blue) **[20a]**.

	Complexes			
Geo. Param.[a]	$[U(Cp^*)_2(SMe)_2]$ (**1**)	$[U(Cp^*)_2(S^tBu)_2]$ (**2**)	$[U(Cp^*)_2(S^iPr)_2]$ (**3**)	$[U(Cp^*)_2(SPh)_2]$ (**4**)
$U–S_1$	2.710 **2.738** (2.730) **2.639**	2.717 (2.709)	2.712 (2.724)	2.732 (2.752)
$U–Ct_1$	2.521 **2.535** (2.560) **2.470**	2.546 (2.570)	2.531 (2.558)	2.515 (2.543)
$S_1–C_1$	1.846 **1.847** (1.859) **1.810**	1.884 (1.901)	1.868 (1.878)	1.792 (1.800)
$S_1–U–Ct_1$	108.2 **109.5** (108.4) **108.4**	106.9 (107.7)	111.6 112.2	111.226 (111.275)
$Ct_1–U–Ct_2$	135.0 **135.7** (134.5) **137.6**	131.0 (131.2)	134.2 (132.9)	134.6 (133.9)
$S_1–U–S_2$	98.7 **87.7** (94.1) **97.2**	106.9 (87.7)	103.0 (102.7)	103.2 (102.680)
$<U–C_{(Cp)}>$	2.790 **2.81** (2.793) **2.73**	2.810 (2.843)	2.794 (2.832)	2.792 (2.820)

[a]Ct_1 and Ct_2 are the Cp* ring centroids.

Thus, the U–S bond lengths of complex **1,** namely 2.710Å as computed at the B3PW91 level, are slightly larger than those measured by X–ray crystallography, 2.639Å in $[U(Cp^*)_2(SMe)_2]$, when using the large–core RECP pseudopotential for uranium metal. The same trend for the other lengths of U–Ct and U–C is observed. For example, for complex **1**, displayed on Figure 2, the carbon atoms of the cyclopentadienyl ring are coplanar; the distance between the uranium atom and the centroid of the Cp* cycle is equal to 2.53 Å in average and is slightly larger than the value of 2.47 Å determined by X–ray crystallography, whereas those between the metal and carbon atoms of the cycle $U–C_{(Cp)}$ are in average equal to 2.79 Å (values in the gas phase), larger than the experimental values by 0.06 Å. On the other hand, the computed angles correctly reproduce those observed in the crystal; as an example, the angles $S_1–U–Ct_1$ and $Ct_1–U–Ct_2$ of 108.2 and 135.0° are very close to the X–ray values which are equal to 108.4 and 137.6°, respectively. Finally, as it can be seen in Table 1, the influence of the THF solvent on the optimized geometrical parameters of complex **1** is rather small, even if we note that the $U–C_t$ and U–S lengths increase slightly in solvent. This result makes us confident that the gas phase optimized geometries are accurate enough for all complexes. The optimized coordinates of all compounds are given in the Supporting Information (Tables SI1) whereas the optimized geometries of $[U(Cp^*)_2(SR)_2]$ (R=Me, ^{t}Bu, ^{i}Pr, Ph)] are depicted on Figure SI2.

We consider now the Wiberg Bond Indices, which are useful tools for the analysis of bonding and of the electronic structure of organometallic complexes. Generally, the calculated WBI correlate very well with experimental data like bond lengths and vibrational frequencies. In Table 2 are reported the WBI of the U–S and S–C bonds and their corresponding lengths computed at the B3PW91 level in the gas phase.

Table 2. WBI of the U–S and S–C Bonds and their Corresponding U–S and S–C Bond Lengths (Values in Parentheses).

Complex	$U–S_1$	$U–S_2$	$S_1–C_1$	$S_2–C_2$
$[U(Cp^*)_2(SMe)_2]$	0.903 (2.710)	0.903 (2.710)	1.004 (1.846)	1.005 (1.846)
$[U(Cp^*)_2(S^tBu)_2]$	0.928 (2.717)	0.928 (2.719)	0.939 (1.884)	0.939 (1.884)
$[U(Cp^*)_2(S^iPr)_2]$	0.915 (2.712)	0.916 (2.714)	0.962 (1.868)	0.963 (1.865)
$[U(Cp^*)_2(SPh)_2]$	0.857 (2.732)	0.856 (2.732)	1.043 (1.792)	1.044(1.790)

As it can be seen, the bisthiolate uranium complexes exhibit single U–S and S–C bonds with bond indexes close to 1. The U–S bonds which are involved in the insertion reaction, exhibit bond indexes lower than 1, varying from 0.857 for R = Ph to 0.928 for R = ^{t}Bu. Identical index orders are observed in all cases for the U–S_1 and U–S_2 bonds, in accordance with the similarity of the U–S_1 and U–S_2 bond lengths. The same observation is noticed in the case of the S_1–C_1 and S_2–C_2 bonds.

Populations analyses of the thiolate uranium(IV) complexes bring light into some other aspects of the metal–ligands interaction. Despite its well known limitations, because of the strong basis-set dependence and the inconsistency of the results when dealing with non-covalent bond as in the case of some metallic complexes, MPA permits generally to describe qualitatively the evolution of charge transfers and bonding interactions occurring in a series of homologous molecular systems, while the NPA analysis, which has been shown to be useful in inorganic chemistry, provides more reliable atomic net charges. In Table 3 are collected the computed MPA and NPA charges of U, X atoms and Cp* ligands of the neutral compounds. By net charges of SR and Cp*, one understands the global charge of the thiolate and the pentamethylcyclopentadienyl ligands respectively, and not only that of the atom connected to uranium.

Table 3. MPA and NPA Charges from B3PW91 Computations in THF.

	MPA / NPA charges				
Complex	U	SR1	SR2	Cp*1	Cp*2
$[U(Cp^*)_2(SMe)_2]$	1.028/1.893	–0.351/–0.428	–0.352/–0.429	–0.164/–0.519	–0.160/–0.517
$[U(Cp^*)_2(S^tBu)_2]$	1.042/1.853	–0.365/–0.420	–0.380/–0.432	–0.156/–0.502	–0.142/–0.499
$[U(Cp^*)_2(S^iPr)_2]$	1.018/1.870	–0.354/–0.431	–0.356/–0.431	–0.159/–0.504	–0.149/–0.504
$[U(Cp^*)_2(SPh)_2]$	0.993/1.899	–0.368/–0.448	–0.368/–0.451	–0.128/-0.501	–0.129/–0.499

The Mulliken analysis (detailed in SI) indicates that the MPA net charges (not the real charges) of the metal are largely smaller than its oxidation state +4 for the neutral compounds due to the ligands–to–metal donation, the latter effect being highlighted by the weak negative charges carried by the Cp* and thiolate ligands. The NPA analysis is supposed to exhibit improved numerical stability and to better describe the electron distribution in molecular systems containing metal atoms compared to the other schemes. As already noticed with MPA, the ligands–to–metal donation is strong for the U(IV) ion; this is highlighted by the decrease of the MPA net charges of the ligands. However, the SR ligands exhibit relatively large negative MPA charge compared to the Cp* ligand and this negative charge is mainly concentrated on

the S atom with a mean value of –0.368 indicating that, despite the covalent aspect of the bonding between the uranium atom and the ligand, the interaction between the uranium and sulfur atoms is more electrostatic in nature than that between U and Cp* which carry MPA charges of 1.020 and –0.151, respectively. However, according to the NPA analysis, these two electrostatic interactions are of the same order of magnitude. Despite this contradiction, these two charge analyses (MPA and NPA) highlight the electrostatic interaction between the uranium atom and the different ligands. The frontier molecular orbitals (FMO), which are of importance when investigating chemical bonding and reactivity, are now considered. The highest occupied molecular orbital (HOMO) and lowest unoccupied molecular orbital (LUMO) of $[U(Cp^*)_2(SMe)_2]$ (**1**) and $[U(Cp^*)_2(S^tBu)_2]$ (**2**) are displayed in Figure SI3. As we note from this figure, the HOMO is composed mainly by the p orbitals of S and C atoms, the contribution of the metal center being negligible, whereas in the LUMO the metal center contributes mainly with the 6d orbitals.

3.2. Reactivity of the bisthiolate uranium(IV) complexes $[U(Cp^*)_2(SR)_2]$ towards CS_2 and CO_2.

The reactivity of the bisthiolate uranium(IV) complexes $[U(Cp^*)_2(SR)_2]$ (R = Me, ^{t}Bu, ^{i}Pr, Ph) with CO_2 and CS_2 is explored using the methodology described below. All obtained stationary points have been fully optimized and were characterized by their frequency using vibrational frequency calculations as minima without any imaginary frequency for ground states, or transition states (TS) with only one imaginary frequency. The IRC calculations confirmed that the found transition states do link the two corresponding minima (of reactants and products).

Experimentally [32], these reactions gave the insertion derivatives $[U(Cp^*)_2(SR)(E_2CSR)]$ (E = O and R = ^{t}Bu; E = S and R = Me, ^{i}Pr or ^{t}Bu) where the molecule CS_2 or CO_2 is inserted into the U–S bond of the reactant complexes. $[U(Cp^*)_2(SMe)_2]$ reacted with CO_2 in THF under mild conditions (1 atm, 20° C) to form several unidentified products whereas $[U(Cp^*)_2(S^tBu)_2]$ reacted very quickly (a few minutes) with CO_2 under the same conditions to form the insertion derivative $[U(Cp^*)_2(O_2CS^tBu)_2]$. Otherwise $[U(Cp^*)_2(SMe)_2]$ reacted with CS_2 in toluene to form after a few hours at 70° C the mono–insertion product $[U(Cp^*)_2(SMe)(S_2CSMe)]$. On the other hand, two days were required to form $[U(Cp^*)_2(S^tBu)(S_2CS^tBu)]$ from $[U(Cp^*)_2(S^tBu)_2]$.

The simple functionalization of CS_2 or CO_2 through the $[U(Cp^*)_2(SR)_2]$ (R = Me, ^{t}Bu, ^{i}Pr, Ph) complexes should proceed in a similar way according to Figure 2 where the reactions of $[U(Cp^*)_2(SMe)_2]$ and CO_2 or CS_2 are depicted.

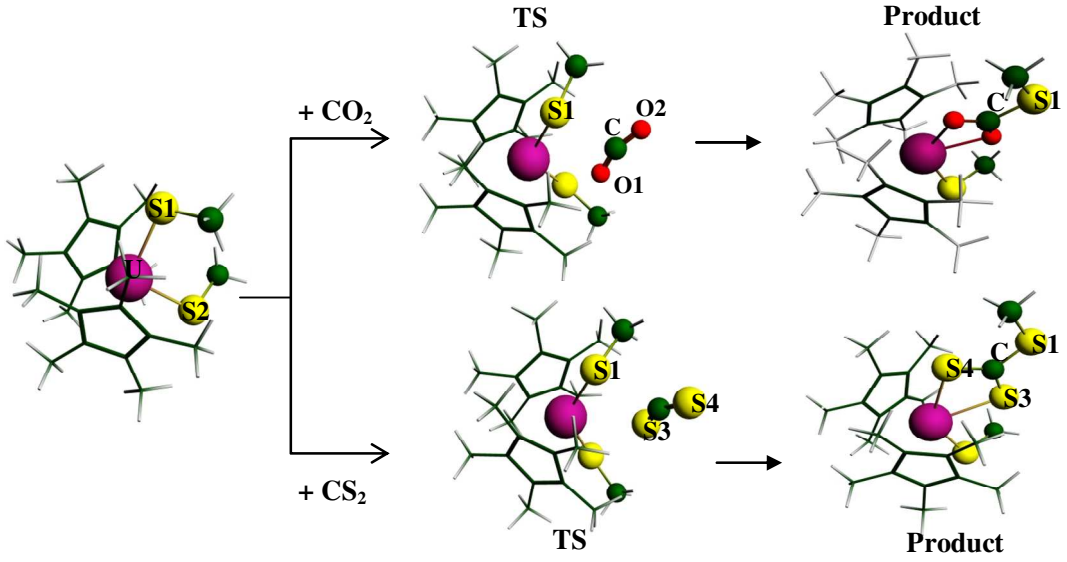

Figure 2. Structures of the species involved in the reaction of $[U(Cp^*)_2(SMe)_2]$ and CX_2 (X = O, S).

In the following sections the characteristics of each reaction in terms of geometries, energies and NBO analysis will be detailed.

3.2.1 Reactivity with CS_2.

The insertion of CS_2 into the U–S bond of the $[U(Cp^*)_2(SR)_2]$ complexes proceeds first by the interaction of CS_2 with the methylthiolate group SR. When the CS_2 carbon atom approaches the sulfur atom of the SR group, one of the C–S bonds is elongated from 1.57 Å in free CS_2 to around 1.61 Å, accompanied by a bending of the molecule of about 156° in the TS structures. In the meantime, the U–S bond is elongated, varying from 2.520 Å for R = Ph to 2.672 Å for R = Me, leading to the breaking of this bond. Then, the $SRCS_2^-$ ligand already formed coordinates to the uranium atom in the η^2–SS mode leading to the formation of the product $[U(Cp^*)_2(SR)(S_2CSR)]$ in which CS_2 is inserted into the U–S bond through the two U–S(CS_2) bonds which exhibit slightly different lengths of 2.97 and 2.91 Å. The other U–S bond lengths which are not involved in the insertion remain unchanged, around 2.766 Å.

We focus now on the reaction of CS_2 with $[U(Cp^*)_2(S^tBu)_2]$ which leads to the uranium trithiocarbonate derivative $[U(Cp^*)_2(S^tBu)(S_2CS^tBu)]$, the only insertion complex which was crystallographically characterized.

.

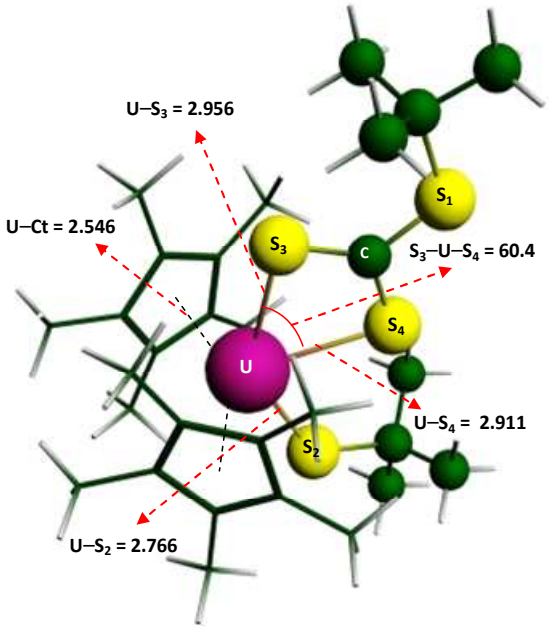

Figure 3. Optimal geometry of the uranium trithiocarbonate complex $[U(Cp^*)_2(S^tBu)(S_2CS^tBu)]$.

The computed geometry of this insertion product (Figure 3) is in good agreement with the X–ray crystal structure. The calculated bond lengths of U–S_2, U–S_3, U–S_4 and U–C_t are respectively 2.766, 2.956, 2.911 and 2.546 Å, whereas the experimental values are 2.643, 2.885, 2.821 and 2.490 Å, respectively. Moreover, the calculated angles are close to the experimental ones. The S_3–U–S_4 bite angle is found to be 60.4° practically identical to the experimental value of 62.0°. However, the computed U–S lengths are slightly overestimated relatively to the experimental ones, as it was already observed for complex **1** (vide supra).

The IRC calculations carried out for the $\{[U(Cp^*)_2(SR)_2] + CS_2\}$ reactions (with R = Me, ^{t}Bu, ^{i}Pr, Ph) showed the nonexistence of any intermediate state IM between the transition state and the reactants (or product). In all reactions for the considered spin state, the TS connects directly the reactants (at IRC backward) and the product (at IRC forward); it can be noticed that the product is always more stable that the reactants (exergonic reactions).

The energy profiles where the relative (to the reactants) enthalpies are considered and which are similar for all the $\{[U(Cp^*)_2(SR)_2] + CS_2\}$ reactions are depicted in Figure 4.

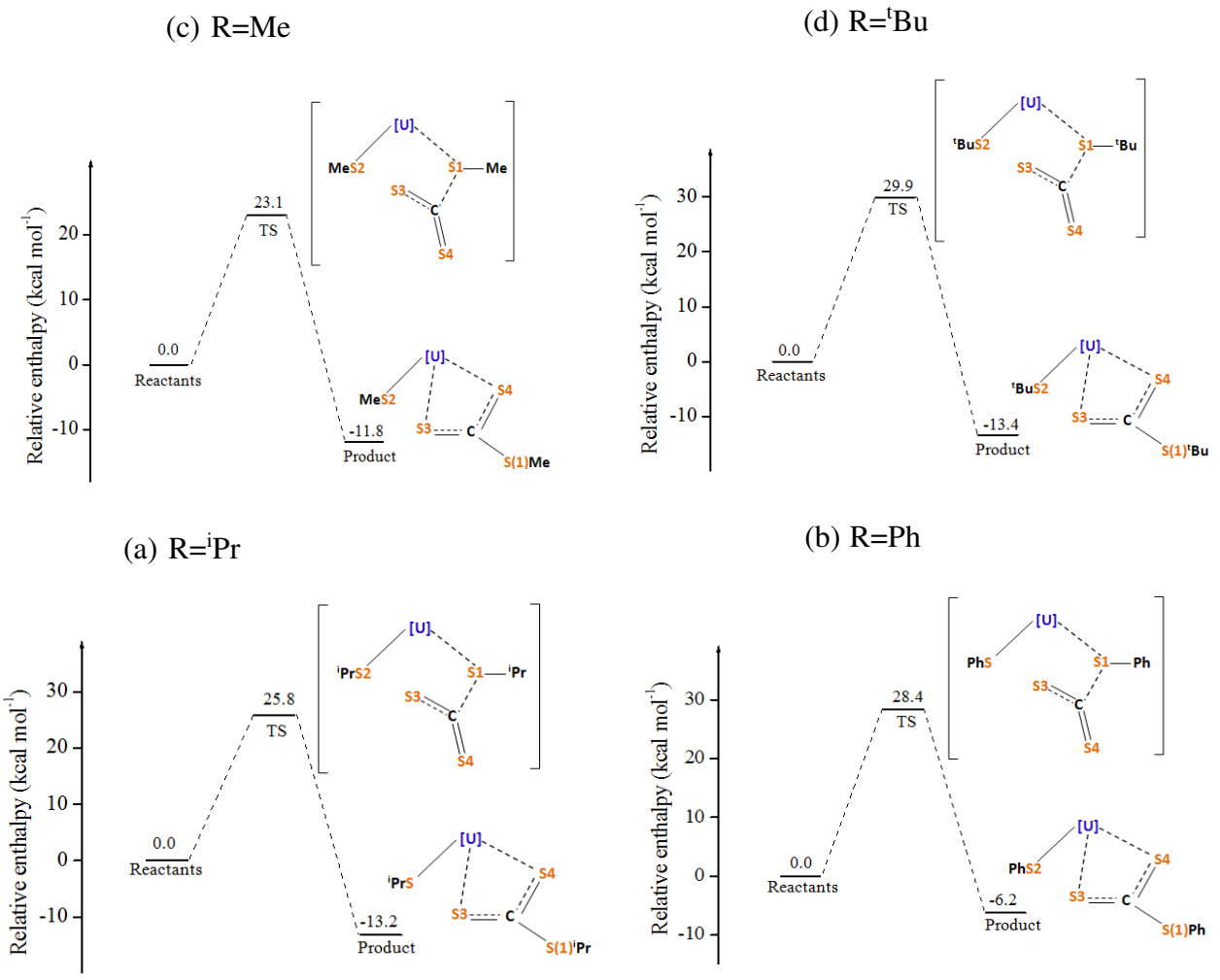

Figure 4. Energy profiles of the {[U(Cp*)$_2$(SR)$_2$] + CS$_2$} reactions in the gas phase.

Figure 4(a) giving the enthalpy profile of the reaction of [U(Cp*)$_2$(SMe)$_2$] with CS$_2$ in the gas phase, brings to light an enthalpy of activation $\Delta H^{\#}$ of 23.1 kcal.mol^{-1} which is the lowest of the four considered reactions. The formation of the insertion product [U(Cp*)$_2$(SMe)(S$_2$CSMe)] is then kinetically favored compared to the other reactions, and also thermodynamically favorable with an exothermic character of 11.8 kcal.mol^{-1}. The reaction of [U(Cp*)$_2$(S^{t}Bu)$_2$] with CS$_2$ seems to be the more difficult to achieve with the largest activation enthalpy (29.9 kcal.mol^{-1}) compared to the other reactions. The exothermic character is estimated to be -13.4, -13.2 and -6.2 kcal.mol^{-1} for R = ^{t}Bu, ^{i}Pr and Ph respectively indicating that the reaction of [U(Cp*)$_2$(SPh)$_2$] and CS$_2$ is the less thermodynamically favorable in this series of reactions.

In Table 4 are reported the relative enthalpies of all stationary points (reactants, TS(s) and product) calculated in the gas phase and in toluene. As indicated in section 2, the used solvation model is the SMD one the dielectric constant of toluene being equal to 2.3741. We note that the insertion reaction is more efficient in toluene since the activation energy is smaller than in the gas phase in all cases, as noted for the {[$U(Cp^*)_2(SMe)_2$] + CS_2} reaction where the reaction energy in toluene drops to 9.2 kcal.mol^{-1} vs. 23.1 kcal.mol^{-1} in the gas phase.

Table 4. Relative Energies of Stationary Points at the B3PW91 Level of Theory: Reactants, Products and Transition States. Values in Parentheses are Relative Energies in Toluene (all Energies are in kcal.mol^{-1}).

	Relative energies			
R	Reactants	TS Activation Energy $\Delta H^{\#}$	Product	Reaction barrier $\Delta G^{\#}$
Me	0 (0)	23.1 (9.2)	– 11.8 (– 24.2)	34.7
^{i}Pr	0 (0)	25.8 (12.6)	– 13.2 (– 25.5)	35.3
Ph	0 (0)	28.4 (15.7)	– 6.2 (– 16.2)	39.3
^{t}Bu	0 (0)	29.9 (18.0)	– 13.4 (– 25.1)	38.9

Otherwise, it is noteworthy that the activation energy $\Delta H^{\#}$ of the different reactions, either in the gas phase or in toluene solvent, is ranked as following: $\Delta H^{\#}$ (Me) < $\Delta H^{\#}$ (^{i}Pr) < $\Delta H^{\#}$ (Ph) < $\Delta H^{\#}$ (^{t}Bu) in accordance with the steric crowding of the R group of the thiolate ligand. According to Marçalo studies **[58]**, the steric coordination numbers of the ligands are ordered as Me (1.06) < ^{i}Pr (1.22) < Ph (1.26) < ^{t}Bu (1.50). Indeed, the electrophilic attack of CS_2 is favored when the SR ligand is less crowded thus facilitating the formation of a C–S bond between the C atom of the carbon disulfide and the S atom of the SR ligand. In addition, the free energy barriers ($\Delta G^{\#}$) are larger than those of activation enthalpies and follow the same trend except for Ph and ^{t}Bu complexes where the free energy barrier of the first one is slightly larger than the second one, i.e. 39.3 vs. 38.9 kcal.mol^{-1}. However, the reaction mechanism of the CS_2 insertion is performed in an identical way for the four reactions, whatever the size of the R group. The first step is characterized by a bending of CS_2 molecule whereas the C (CS_2) and S_1 (SR) atoms get closer, accompanied by the lengthening of the C–S_3 bond and the beginning of the formation of the U–S_3 bond. The effective breaking of the U–S_1 bond comes only in the second step, when the TS barrier is overcome, accelerating thus the formation of the

U–S_3 and U–S_4 bonds; it is worth noting that the formation of the U–S_3 bond occurs first, the formation of U–S_4 bond occurring by the reorientation of the CS_2 molecule.

FMO analysis of the {[U(Cp*)$_2$(SR)$_2$] + CS$_2$} reactions.

Analysis of the frontier molecular orbitals (FMOs) of the TS of the {[U(Cp*)$_2$(SR)$_2$] + CS_2} gas–phase reactions has been carried out (Figure 5). The diagram illustrates the contribution to FMOs of four components: the (Cp*)$_2$ and (SR)$_2$ orbitals, the U orbitals and the CS_2 orbitals, as well as the FMOs energies. The HOMOs are mainly composed of the ligand (SR)$_2$ atomic orbitals in all transition state structures, the largest value, 62%, being observed in the case of the {[U(Cp*)$_2$(SMe)$_2$] + CS_2} reaction which exhibits the lowest activation barrier (34.7 kcal.mol^{-1}) and the smallest value of 43% corresponds to the {[U(Cp*)$_2$(SPh)$_2$] + CS_2} reaction which exhibits the highest activation barrier (39.3 kcal.mol^{-1}). The other transition states exhibit intermediate compositions, 52 and 53% for the reaction of [U(Cp*)$_2$(S^{t}Bu)$_2$] and [U(Cp*)$_2$(S^{i}Pr)$_2$] with CS_2 respectively, with intermediate activation barriers. The contribution of the uranium orbitals to the HOMO is negligible as well as those of CS_2 whereas the (Cp*)$_2$ orbitals contribute with a small weight of 13% in the TS of the {[U(Cp*)$_2$(S^{t}Bu)$_2$] + CS_2} reaction. However, it is worth noting that the uranium orbitals are involved in lower energy occupied orbitals, corresponding to the bonding between the metal and the surrounding ligands.

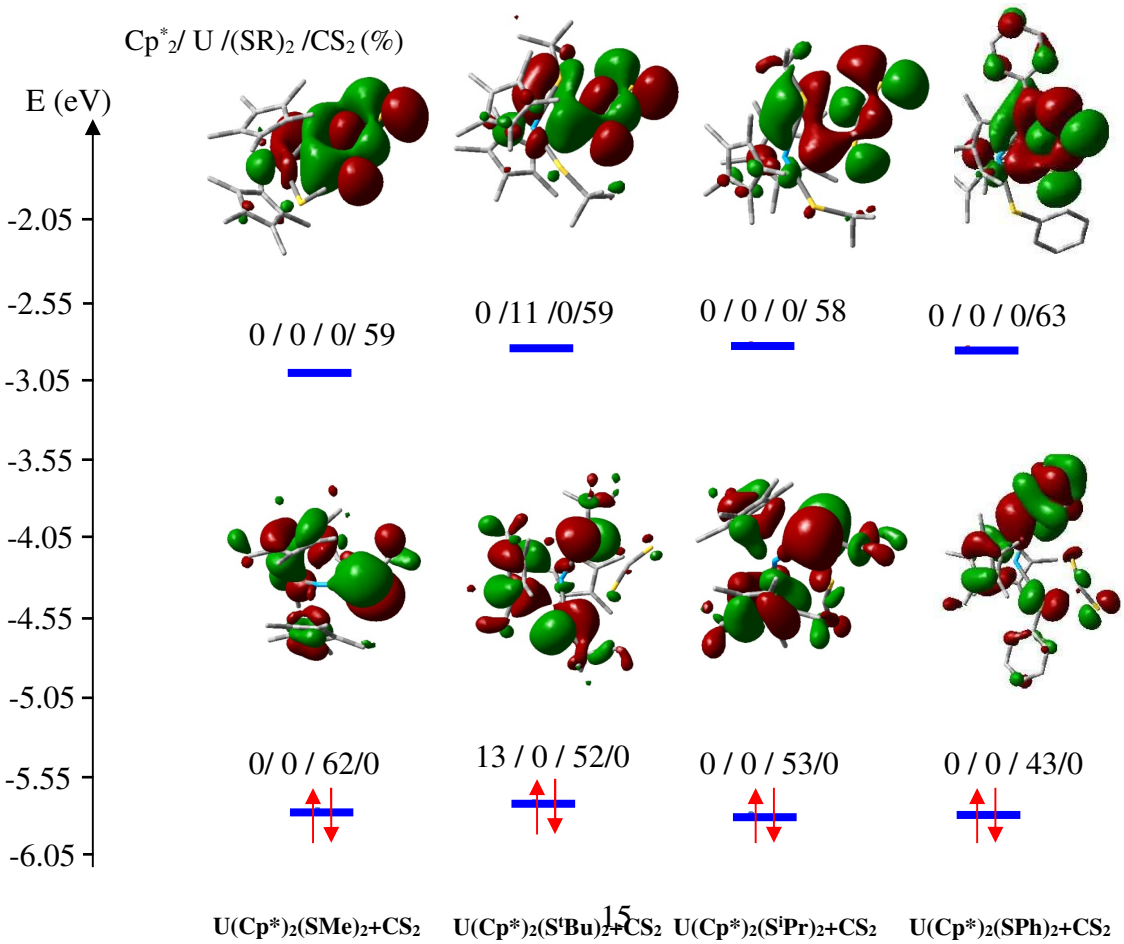

Figure 5. FMO diagram of the transition states of the {[U(Cp*)$_2$(SR)$_2$] + CS_2} reactions with the contribution of the (Cp*)$_2$/U/(SR)$_2$/CS_2 atomic orbitals to FMOs.

Contrarily to the HOMOs, the LUMOs are mainly composed of CS_2 orbitals and the contribution of the (SR)$_2$ orbitals to the LUMO is negligible for the four reactions. The largest value of 63% is observed for the TS of the {[U(Cp*)$_2$(SPh)$_2$] + CS_2} reaction which is the less efficient and the other values are lower but close, 59% for the {[U(Cp*)$_2$(SMe)$_2$] + CS_2} and {[U(Cp*)$_2$(S^{t}Bu)$_2$] + CS_2} reactions, and 58% for the {[U(Cp*)$_2$(S^{i}Pr)$_2$] + CS_2} reaction. The Kohn–Sham HOMO–LUMO gap for the four TSs is close to 3.2 eV in average.

The reaction process has also been investigated using WBI and NPA analyses, two tools providing interesting insights into evolution of the CS_2 insertion. In Table 5 are given the WBI of selected bonds involved in the insertion process, computed in the gas phase at the B3PW91 level of theory.

Table 5. Computed WBI for the U–S$_i$ and C$_3$–S$_i$ Bonds for the {[U(Cp*)$_2$(SR)$_2$] + CS_2} reactions (R = Me, ^{t}Bu, ^{i}Pr and Ph).

	<U–S$_1$>	<U–S$_2$>	<C$_3$–S$_3$>	<C$_3$–S$_4$>	< C$_3$–S$_1$>	<U–S$_3$>	<U–S$_4$>
Reactants	0.901	0.900	1.973	1.973	–	–	–
TS	0.694	0.865	1.650	1.977	0.229	0.484	0.026
Product	0.034	0.868	1.313	1.340	0.941	0.607	0.557

According to Table 5, the WBI mean values of the U–S$_1$ bond of the [U(Cp*)$_2$(SR)$_2$] complexes and of the C$_3$–S$_3$ bond of CS_2 decrease from 0.901 and 1.973 to 0.694 and 1.650 respectively in the transition states, in accordance with the increase of their corresponding bond lengths, showing that these bonds become weaker. On the other hand, we note the formation of a weak bond between the uranium and one of the CS_2 sulfur atoms, i.e. U–S$_3$, for which the WBI is equal to 0.484. In parallel, bonding between the carbon atom C$_3$ of CS_2 and the S$_1$ sulfur atom of [U(Cp*)$_2$(SR)$_2$] begins to take place, presenting a WBI equal to 0.229. The final products exhibit single bonds with WBI close to 1, except for the inserted two sulfur atoms S$_3$ and S$_4$ bonded to the uranium for which the bond indexes are slightly different, being equal respectively to 0.607 and 0.557. These variations are in accordance with their bond lengths, the lower WBI corresponding to the larger bond length.

The NPA results are depicted in Figure 6 where the net charges (which are not the real ones) of relevant atoms, namely U, S_1 of SR and the mean charge value of S_3 and S_4 of CS_2 are reported, for the {[$U(Cp^*)_2(SMe)_2$] + CS_2} gas–phase reaction. Thus, the NPA net charges of uranium and S_1 (of SR group) atoms in [$U(Cp^*)_2(SMe)_2$] are around 1.90 and –0.36 respectively whereas in the CS_2 molecule, the carbon is negatively charged (–0.464) and the sulfur atoms (S_3 and S_4) are positively charged (identical value of 0.231). When reaching the transition state, the NPA charge of uranium decreases revealing electronic charge transfer from ligand to uranium. At the same time the net charge of the S_1 atom increases revealing a loss of electronic density. The two sulfur atoms S_3 and S_4 of CS_2 exhibit the same trend during the different steps of the reaction, with a decrease of the NPA net charge to reach a negative value of –0.05 and –0.02 in the final product. These final insertion products derived from the reaction with CS_2 exhibit for the uranium atom a NPA charge of 1.73, smaller than the initial charge, and for the carbon atom a charge of –0.604.

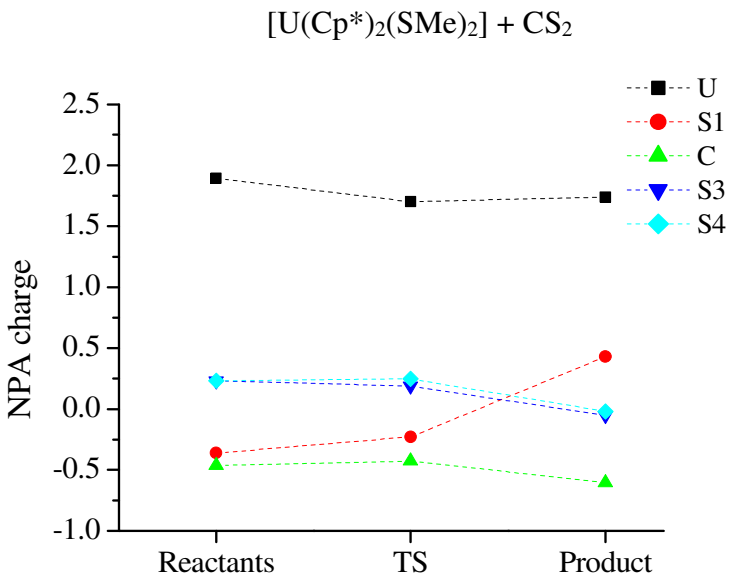

Figure 6. NPA charges evolution along the {[$U(Cp^*)_2(SMe)_2$] + CS_2} reaction.

3.2.2 Reactivity with CO_2

The mechanism of the CO_2 insertion reaction proceeds in a similar way than that of CS_2 except that the C (CO_2) and S (SR) atoms get closer due to the electrostatic attraction between the positively charged carbon and the negatively charged sulfur. Thus, in the first step, the carbon

dioxide interacts spontaneously with the SR group leading to the loss of the linearity of CO_2 reaching a bond angle around 158° in the TS(s) and the formation of a C–S bond accompanied by the lengthening of the C–O bond from 1.160 Å in free CO_2 to around 1.195 Å in TS(s). In parallel, the U–S bond involved in the insertion reaction is slightly elongated from ca. 2.5 Å to reach a value around 2.8 Å leading to the breaking of this bond. The insertion products $[U(Cp^*)_2(SR)(O_2CSR)]$ are obtained by the coordination of the $SRCO_2^-$ ligand to the uranium atom in an η^2–OO mode presenting two U–O bonds slightly different (2.47 Å and 2.52 Å).

The analysis of the CO_2 insertion reaction from the energy point of view is illustrated through the calculated energy profiles in terms of the relative enthalpies for the four $\{[U(Cp^*)_2(SR)_2] + CO_2\}$ gas–phase reactions which are reported in Figure 7. As the experimental reactions of these complexes with CO_2 have been done in the THF solvent, the effect of this solvent (dielectric constant of 7.4257) has been considered using the SMD continuum solvation model.

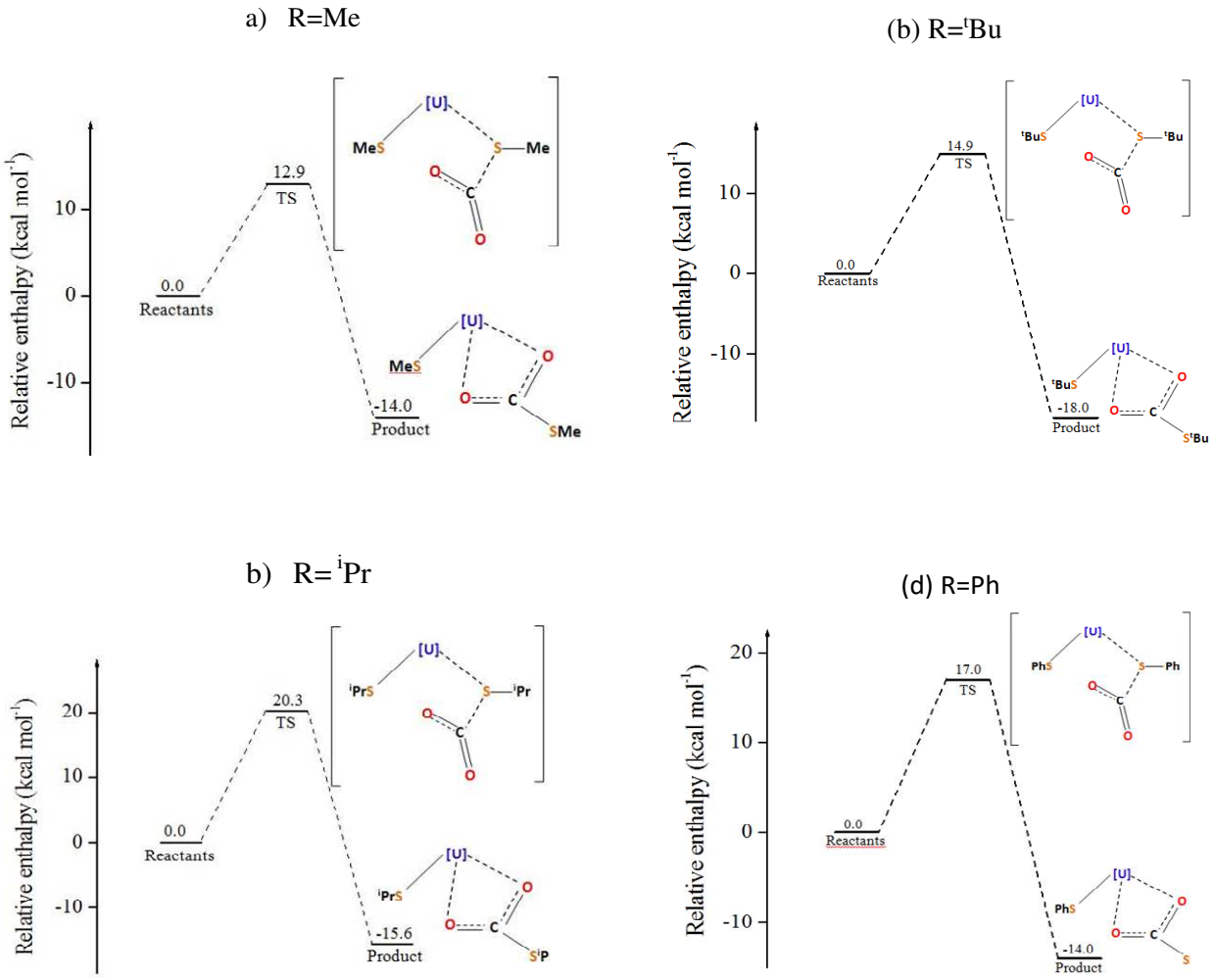

Figure 7. Energy profiles for the $\{[U(Cp^*)_2(SR)_2] + CO_2\}$ gas–phase reactions: (a) R=Me, (b) R=^{t}Bu (c) R=^{i}Pr and (d) R=Ph.

In Table 6 are given the enthalpy energies of all species involved in the {[U(Cp*)$_2$(SR)$_2$] + CO_2} reactions, i.e. reactants, TS and products, computed in the gas phase and in THF (used for the reaction with CO_2) at the B3PW91 level of theory.

Table 6. Relative Enthalpy Energies of Stationary Points at the B3PW91 Level of Theory of the {[U(Cp*)$_2$(SR)$_2$] + CO_2} Reactions: Reactants, Transition States and Products (Values in Parentheses are Determined in THF, Given in kcal.mol^{-1}).

	Relative enthalpy energy			
R	Reactants	TS Activation Energy $\Delta H^{\#}$	Product	Reaction barrier $\Delta G^{\#}$
Me	0 (0)	12.9 (7.8)	–14.0 (–15.7)	22.5
^{i}Pr	0 (0)	20.3 (13.9)	–15.6 (–16.9)	29.9
Ph	0 (0)	17.0 (11.0)	–9.3 (–8.5)	26.6
^{t}Bu	0 (0)	14.9 (7.9)	–18.0 (–19.6)	23.7

As in the case of the reaction with CS_2, the {[U(Cp*)$_2$(SMe)$_2$] + CO_2} reaction in the gas phase exhibits the lowest energy barrier with a value of 12.9 kcal.mol^{-1}, indicating the efficiency of this reaction which exhibits an exothermic enthalpy of –14.0 kcal.mol^{-1}. The R = ^{i}Pr group leads to the highest enthalpy barrier equal to 20.3 kcal.mol^{-1} but lower than that of the corresponding reaction with CS_2 which gave a barrier height equal to 25.8 kcal.mol^{-1}. The other reactions exhibit an intermediate accessible activation energy, 14.9 and 17.0 kcal.mol^{-1} for {[U(Cp*)$_2$(SR)$_2$] + CO_2}reactions, with R = ^{t}Bu and Ph, respectively. As in the reactions with CS_2, reactions of the bisthiolate uranium complexes with CO_2 depend of the steric hindrance of the R ligands, more the R steric hindrance is large more the reaction is difficult. One can see in Table 6 that the THF solvent does not affect the trend of energies but affects the values, the activation barriers and the reaction energies are much smaller than those obtained in the gas phase. From 12.9 and 20.3 kcal.mol^{-1} in the gas phase, the activation energy drops to 7.8 and 13.9 kcal.mol^{-1}respectively, the differences being estimated about 40%. Solvation facilitates the reactions.

Regarding the Wiberg Bond Indexes of the U–S bonds, the same trend as for the reaction with CS_2 is observed for the CO_2 insertion reaction. The U–S_1, C_3–O_1 and C_3–O_2 WBI decrease along the insertion reaction, from 0.903, 1.881, 1.881 respectively for the free reactants to 0.713, 1.288, 1.380 in the transition state in the case of the {U(Cp*)$_2$(SMe)$_2$ + CO_2} reaction

(Figure 8). In the transition state, the WBI of the C–O bonds are different; one is smaller than the second indicating that the first C–O bond elongates allowing the formation of the first U–O bond, whereas the S_1–C_3 WBI increases revealing the beginning of bonding between S_1 and C_3. The final products exhibit single bonds, the C_3–O_1 and C_3–O_2 bonds have the largest WBI, close to 1.3, indicating that these bonds are very strong.

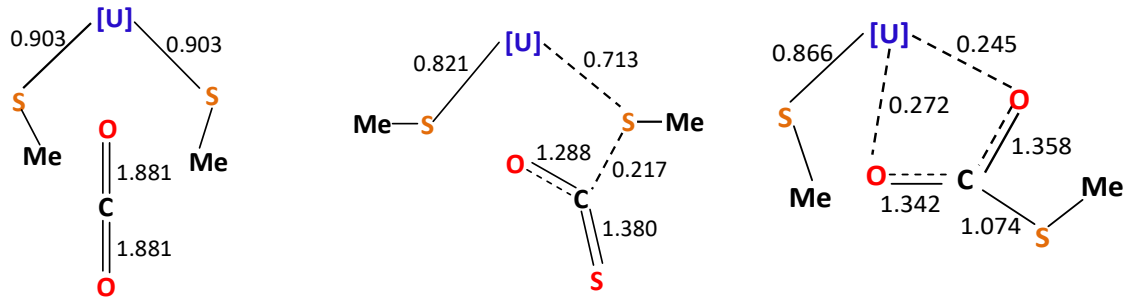

Figure 8. Computed WBI for the {[U(Cp*)$_2$(SMe)$_2$] + CO_2}gas–phase reaction (from left to right, reactant, transition state and product).

As mentioned above, the electrostatic attraction between S_1 and C of CO_2, initiating the insertion reaction, is highlighted through the NPA charge analysis, as illustrated with the {[U(Cp*)$_2$ (SMe)$_2$] + CO_2} gas–phase reaction (Figure 9). In the first step (free reactants), the carbon atom of CO_2 possesses a positive charge (1.038) whereas the S_1 atom exhibits a negative charge (–0.362). We note also the charge alternation on the uranium atom (around 1.900) and oxygen atom (–0.519). From reactants to TS, the charges vary slightly whereas a noticeable charge variation occurs between TS and the product. The charge of uranium increases to reach a value around 2.170, exceeding the initial value, the same trend but in opposite direction is observed for the oxygen atom. The latter atom possesses a NPA charge of –0.519 in the free CO_2 molecule which reaches the value of –0.743 in the insertion product passing by the value of –0.513 in the TS.

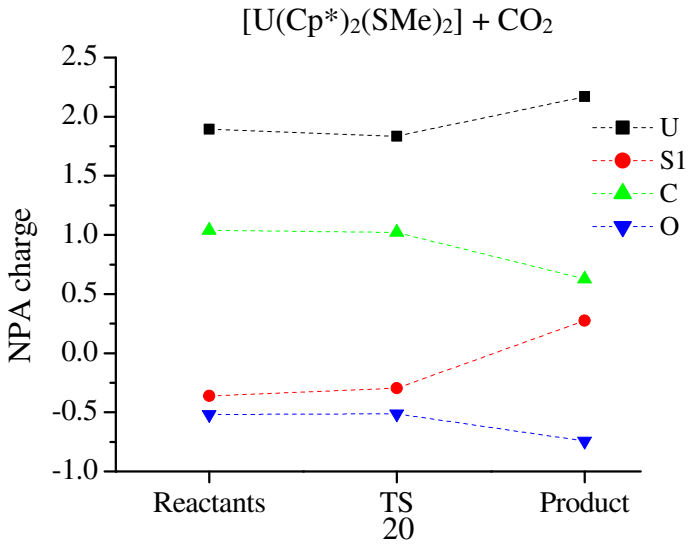

Figure 9. NPA charges evolution along the {[U(Cp*)$_2$(SMe)$_2$] + CO_2} gas–phase reaction.

FMO analysis of the {[U(Cp*)$_2$(SR)$_2$] + CO_2} reactions

The FMO diagram of the TSs of the {[U(Cp*)$_2$(SR)$_2$] + CO_2} gas–phase reactions is displayed in Figure SI6; are given the contributions to the HOMO and LUMO of the atomic orbitals of the four components : (Cp*)$_2$ and (SR)$_2$ ligands, the uranium atom and the CO_2 molecule in place of CS_2 in the preceding reactions. According to this diagram, it is noteworthy that the (SR)$_2$ orbitals participate strongly to both HOMO and LUMO, in contrast to that observed in the insertion of CS_2 where strong participation is noted only to the HOMO. By comparison with the reaction with CS_2, the contribution of the uranium orbitals is larger, especially in the HOMO where it reaches 20% in the case of the {[U(Cp*)$_2$(SMe)$_2$] + CS_2} reaction. Also the contribution of the CO_2 molecule is globally negligible compared to that observed for CS_2 which reaches 63% in the LUMO.

3.2.3 Comparison of the CS_2 and CO_2 insertions into the U–S bond of the bisthiolate complexes.

According to the results discussed above, we note that the reactions of [U(Cp*)$_2$(SR)$_2$] with CO_2 are more efficient than those with CS_2. Indeed, the {[U(Cp*)$_2$(SMe)$_2$] + CS_2} reaction have to overcome a high energetic barrier (23.1 kcal.mol^{-1}) compared to the same reaction with CO_2 where the barrier energy is much smaller (12.9 kcal.mol^{-1}). The reaction mechanism is identical in the two insertion reactions in view of their energy profiles. The transition state links directly the reactant and the product without any intermediate between them. However, differences occur during the reaction processes. The NPA atomic charge distributions are different for the CO_2 and CS_2 insertion reactions. Indeed, in addition to the oxophilic character of the uranium atom, the alternation of charges (Figure 10) in the {[U(Cp*)$_2$(SMe)$_2$] + CO_2} reaction where the C(CO_2) atom is positively charged (1.038), the S$_1$(SR) atom is negatively charged (around –0.362), the U atom is positively charged (around 1.870) and the O atom negatively charged (around –0.520), promote this reaction contrarily to the reaction with CS_2 where the C atom is negatively charged about –0.464 and S positively charged (0.231). This charge alternation is also observed in the transition state and in the final product, the oxygen atoms acquiring a large negative charge (around –0.700) when the uranium exhibits a charge of

around 2.170. Thus, the U–O bonds exhibit a pronounced ionic character compared to the U–S bonds where the charges of the sulfur atoms are equal to –0.05 and –0.03.

a) $[U(Cp^*)_2(SMe)_2] + CO_2$

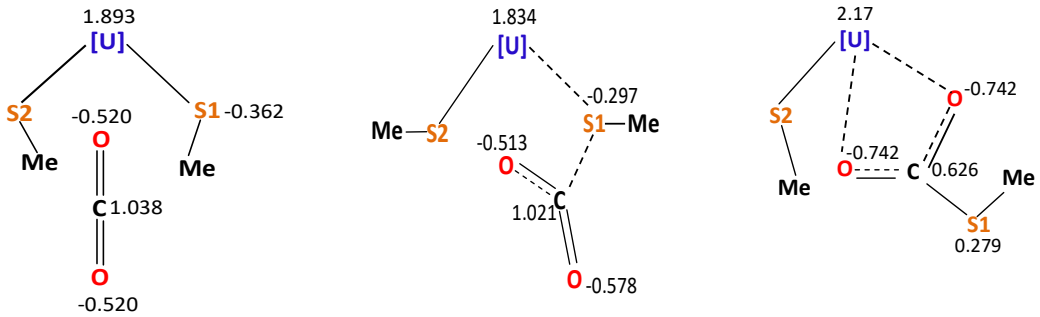

b) $[U(Cp^*)_2(SMe)_2] + CS_2$

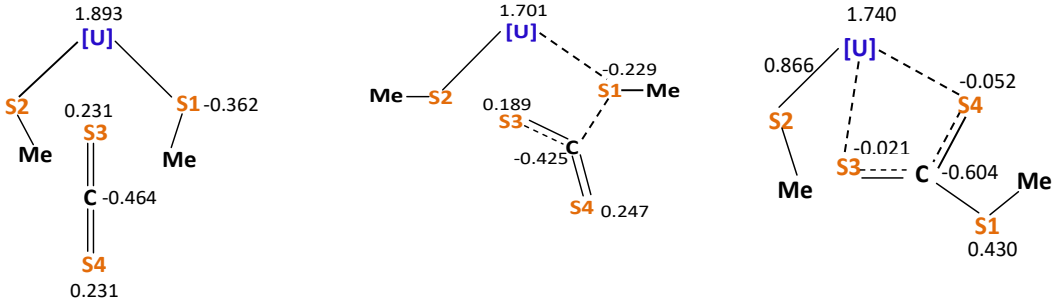

Figure 10. NPA charge distribution on different atoms during the reactions of $[U(Cp^*)_2(SMe)_2]$ with CO_2 (a) and CS_2(b) (from left to right, reactants, TS and product).

It seems interesting to compare the CS_2 and CO_2 insertion in uranium thiolate complexes to the analogous reactions of these molecules with transition metal thiolate compounds. In the transition metal series, it seems that the CS_2 insertion reaction is more favored than that of CO_2. Indeed, the reactivity of ruthenium and tungsten thiolate complexes ($[Ru(Cp)(PPh_3)(SR)]$ and $[W(Cp)(CO_2)(PPh_3)(SR)]$ respectively) toward CS_2 and CO_2 which have been explored by Shaver and co-workers **[59, 60]** and confirmed later by Arroyo *et al.* **[61]** showed the facile insertion of CS_2 into the Ru–SR bond to give the thioxanthate complexes $[Ru(Cp)(PPh_3)(S_2CSR)]$ and into the W–SR bond to give the thioxanthate complexes $[W(Cp)(CO_2)(S_2CSR)]$ while the reaction of CO_2 with $[W(Cp)(CO_2)(PPh_3)(SCHMe_2)]$ could not be confirmed. This reactivity is explained by the electrophilic attack by the pre-coordinated or free CS_2 onto the sulfur atom of the thiolate ligand. This explanation was also reported by Arroyo for the insertion reactions of CS_2 with $[M(SR)_3(PMe_2Ph)_2]$ (M = Ru, Os, R = C_6F_5, C_6F_4H–4). On the contrary, in the case of the uranium bisthiolate complexes under study, as

observed experimentally, the calculations show that the CO_2 insertion into the U–S bond is more favored than the CS_2 insertion regarding the activation energies. When dealing with uranium thiolate complexes it seems that the reactivity of CS_2 and the CO_2 which differs from that with transition metal thiolate complexes is probably due to the oxophilic character of uranium, favoring the CO_2 insertion. The facile insertion reaction in the $[U(Tp^*)_2(CH_2Ph)]$ complex of CO_2 compared to that of CS_2 is also noted by Ding *et al.* **[19]**; in their DFT theoretical study the uranium atom is described by a quasi-relativistic 5f–in–core ECP basis. This insertion reaction is characterized by a low activation barrier equal to 9.5 kcal.mol^{-1} compared to that of CS_2 i.e. 25.0 kcal.mol^{-1}.

3.2.4 Bi–insertion with CS_2 and CO_2

The insertion reactions of the CO_2 and CS_2 molecules into the remaining U–S^{t}Bu bond of $[U(Cp^*)_2(S^tBu)(S_2CS^tBu)]$ (the product of the CS_2 mono–insertion) are now investigated in gas–phase using the methodology described above. The energy profile of these reactions in the gas phase is depicted in Figure 11. As expected, due to the oxophilicity of uranium and the charge alternation between the principal atoms, the activation energy for the insertion of a second CO_2 molecule (1.9 kcal.mol^{-1}) is much smaller than that with CS_2 (27.1 kcal.mol^{-1}). Thus, the CO_2 insertion is more efficient, in accordance with the experimental observation where it was noted that the second insertion of CO_2 was much faster than the CS_2 insertion and was complete after 30 min under normal conditions. Thermodynamically, this reaction is also more favorable with an exothermicity of –27.2 kcal.mol^{-1}. The TS structures are similar to those observed in the mono–insertion reactions except that in the CS_2 bi–insertion reactions, one U–S bond of the U(S_2CS^tBu) fragment is broken (U–S distance equal to 5.30 Å) but is restored at the end of the reaction (U–S distance of 3.09 Å).

a) $[U(Cp^*)_2(S^tBu)(S_2CS^tBu)] + CS_2$

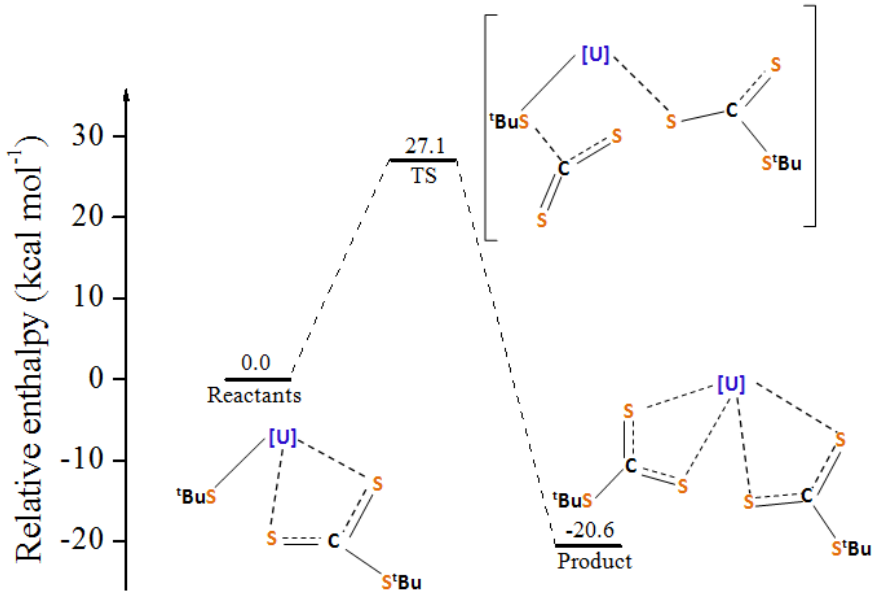

b) $[U(Cp^*)_2(S^tBu)(S_2CS^tBu)] + CO_2$

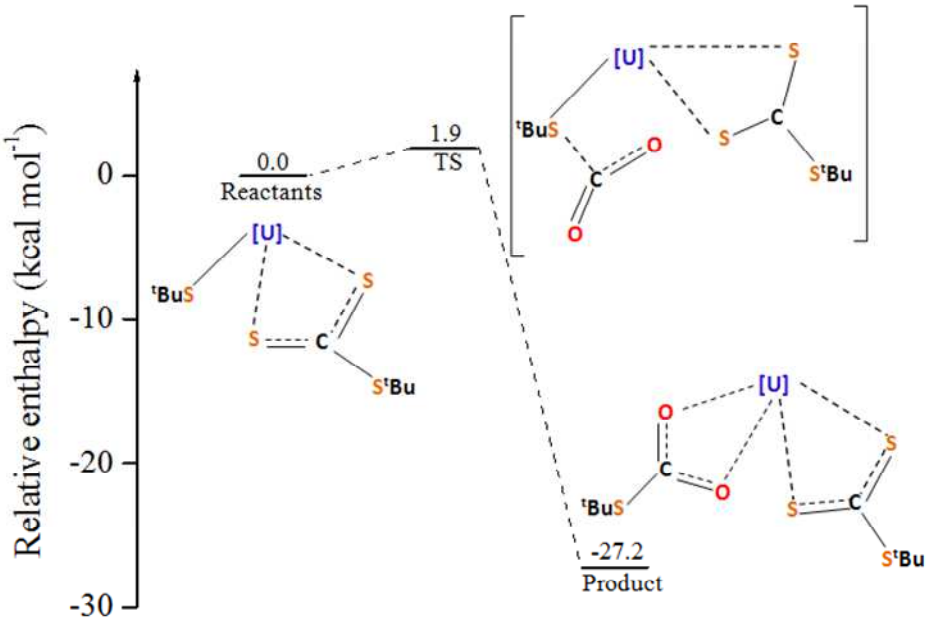

Figure 11. Energy profiles of the bi–insertion gas–phase reactions of $[U(Cp^*)_2(S^tBu)(S_2CS^tBu)]$ with CS_2 (a) and CO_2 (b).

4. Conclusion.

This work describes the structural properties of a series of bispentamethylcyclopentadienylbisthiolateuranium(IV) complexes $[U(Cp^*)_2(SR)_2]$ (R=Me (**1**), ^{t}Bu (**2**), ^{i}Pr (**3**), Ph (**4**)) and their reactions with CO_2 or CS_2 leading to their insertion into the U–S bond, using DFT/B3PW91 computations. The optimized geometries of $[U(Cp^*)_2(SR)_2]$ and the insertion derivative of **2** $[U(Cp^*)_2(S^tBu)(S_2CS^tBu]$ are found in good agreement with the X–ray crystal data. Adducts and transition states structures have been characterized and confirmed by IRC calculations. The steric and electronic factors of the R ligands play a significant role in the reactivity of the $[U(Cp^*)_2(SR)_2]$ compounds; thus, it is more difficult to carry out the insertion reactions for the complex carrying the most sterically demanding S^{t}Bu ligands (complex **2** exhibits the highest activation barrier), in accordance with the steric coordination number of the R group. With the exception of **2**, all thiolate complexes promote the spontaneous carbon dioxide reduction to give the corresponding thiocarbonato complexes. Finally, the computed activation barriers of these reactions show that insertion of CO_2 into the U–S bond of the thiolate complexes is easier and faster than that of CS_2, in agreement with the experimental observation. This distinct (best) reactivity of carbon dioxide is explained by the greatest electronegativity of O, thus allowing a good alternation of charges in the transition states, and by the well-known oxophilic character of uranium which favors initial coordination of CO_2 onto the metal center, before migration of the SR group. The NPA analysis shows that the insertion reaction of CO_2 is favored by the electrostatic attraction between the positively charged C atom and the negatively charged S atom of the SR ligand, leading to the formation of U–O bonds of more ionic character than the U–S bonds formed in the CS_2 insertion reaction. On the contrary, it has been pointed out that in the case of transition metal thiolate complexes the insertion of CS_2 is easier than the CO_2 insertion.

Appendix A. Supporting Information

SI.1: Optimized coordinates for isolated molecules

SI.2: Optimized structures of all complexes

SI.3: Frontier molecular orbitals of $[U(Cp^*)_2(SMe)_2]$ and $[U(Cp^*)_2(S^tBu)_2]$.

SI.4: Wiberg Bond Indices Analysis

SI.5: NPA Charges Analysis

SI6: FMO diagram of transition states of the $\{[U(Cp^*)_2(SR)_2] + CO_2\}$ reactions

Author Information:

Corresponding Authors

E-mail: azizelkechai@yahoo.fr

E-mail: abdou.boucekkine@univ-rennes1.fr.

ORCID

Abdou Boucekkine: 0000-0002-3714-7191

Aziz Elkechai: 0000-0003-0808-6120

Note

The authors declare no competing financial interest.

Acknowledgments

The authors acknowledge the financial support from the Algerian Project CNEPRU n° B00L02UN150120130025. Computing facilities were provided by ASELKAM Computer Center (UMMTO, Algeria). The authors are grateful to GENCI–IDRIS and GENCI–CINES for an allocation of computing time (Grant No. *2017–2018–080649).* The COST CM-1006 action is also acknowledged.

This paper is dedicated to Dr. Jean-François Halet, CNRS Director of Research at the 'Institut des Sciences Chimiques de Rennes, France', on the occasion of his 60th birthday.

References

1. J.A. Labinger, J.E. Bercaw, Nature 417 (2002) 507–514.
2. H. Arakawa, M. Aresta, J.N. Armor, M.A. Barteau, E.J. Beckman, A.T. Bell, J.E. Bercaw, C. Creutz, E. Dinjus, D.A. Dixon, K. Domen, D.L. Dubois, J. Eckert, E. Fujita, D.H. Gibson, W.A. Goddard, D.W. Goodman, J. Keller, G.J. Kubas, H.H. Kunq, J.E. Lyons, L.E. Manzer, T.J. Marks, K. Morokuma, K.M. Nicholas, R. Periana, L. Que, J. Rostrup–Nielson, W.M.H. Sachtler, L.D. Schmidt, A. Sen, G.A. Somorjal, P.C. Stair, B.R. Stults, W. Tumas, Chem. Rev. 101 (2001) 953–996.
3. J. Burdeniuc, B. Jedlicka, R.H. Crabtree, Chem. Ber. Recueil 130(1997) 145–154.
4. B. Wayland, X. Fu, Science 311 (2006) 790 – 791.

5. (a) P.J. Fagan, J.M. Manriquez, E.A. Maatta, A.M. Seyam, T.J. Marks, J. Am. Chem. Soc. 103 (1981) 6650–6667. (b) J.M. Manriquez, P.J. Fagan, T.J. Marks, J. Am. Chem. Soc. 100 (1978) 3939–3941. (c) K.G. Moloy, T.J. Marks, Inorg. Chim. Acta 110 (1985) 127–131. (d) M. Ephritikhine, Organometallics 32 (2013) 2464–2488. (e) M. Ephritikhine, Coord. Chem. Rev. 319 (2016) 35–62.

6. a) W.J. Evans, C.A. Seibel, J.W. Ziller, Inorg. Chem. 37 (1998) 770–776. (b) W.J. Evans, J.M. Perotti, J.C. Brady, J.W. Ziller, J. Am. Chem. Soc. 125 (2003) 5204–5212.

7. O.P. Lam, F.W. Heinemann, K. Meyer, Angew. Chem. Int. Ed. 50 (Ed. 2011) 5965–5968.

8. A. Dormond, A.A. Elbouadili, C. Moise, J. Chem. Soc. Chem. Commun. (1984) 749–751.

9. (a) W.J. Evans, J.R. Walensky, J.W. Ziller, A.L. Rheingold, Organometallics 28 (2009) 3350–3357. (b) W.J. Evans, N.A. Siladke, J.W. Ziller, Chem. Eur. J. (2010) 796–797.

10. (a) K.C. Jantunen, C.J. Burns, I. Castro–Rodriguez, R.E. Da Re, J.T. Golden, D.E. Morris, B.L. Scott, F.L. Taw, J.L. Kiplinger, Organometallics 23 (2004) 4682–4692. (b) J.A. Pool, B.L. Scott, J.L. Kiplinger, J. Am. Chem. Soc. 127 (2005) 1338–1339.

11. a) J.G. Brennan, R.A. Andersen, A. Zalkin, Inorg. Chem. 25 (1986) 1756–1760. (b) I. Castro–Rodriguez, H. Nakai, L.N. Zakharov, A.L Rheingold, K. Meyer, Science 305 (2004) 1757–1759. (c) J.G. Brennan, R.A. Andersen, A. Zalkin, Inorg. Chem. 25 (1986) 1761–1765.

12. (a) J.C. Berthet, J.F. Le Maréchal, M. Nierlich, M. Lance, J. Vigner, M. Ephritikhine, J. Organomet. Chem. 408 (1991) 335–341. (b) I. Castro–Rodriguez, K. Meyer, J. Am. Chem. Soc. 127 (2005) 11242–11243.

13. S.M. Mansell, N. Kaltsoyannis, P.L. Arnold, J. Am. Chem. Soc. 133 (2011) 9036–9051.

14. (a) O.T. Summerscales, F.G.N. Cloke, P.B. Hitchcock, J.C. Green, N. Hazari, Science 311 (2006) 829–831. (b) O.T. Summerscales, F.G.N. Cloke, P.B. Hitchcock, J.C. Green, N. Hazari, J. Am. Chem. Soc. 128 (2006) 9602–9603. (c) P.L. Arnold, Z.B. Turner, R.M. Bellabarda, R.P. Tooze, Chem. 2 (2011) 77–79. (d) B.M. Gardner, J.C. Stewart, A.L. Davis, J. McMaster, W. Lewis, A.J. Blake, S.T. Liddle, Proc. Natl. Acad. Sci. U.S.A. 109 (2012) 9265–9270. (e) A.S. Frey, F.G.N. Cloke, P.B. Hitchcock, I.J. Day, J.C. Green, G. Aitken, J. Am. Chem. Soc. 130 (2008) 13816–13817. (f) G.J. Brennan, R.A. Andersen, J.L. Robbins, J. Am. Chem. Soc. 108 (1986) 335–336.

15. (a) P. Russel, P.J. Scott, J. Am. Chem. Soc. 120 (1998) 1070–1071. (b) F.G.N. Cloke, P.B. Hitchcock, J. Am. Chem. Soc. 124 (2002) 9352–9353.

16. N. Tsoureas, O.T. Summerscales, F.G.N. Cloke, S.M. Roe, Organometallics 32 (2013) 1353–1362.

17. (a) V. Mougel, C. Camp, J. Pécaut, C. Copéret, L. Maron, C.E. Kefalidis, M. Mazzanti, Angew. Chem. Int. Ed. 51 (2012) 12280–12284. (b) O. Cooper, C. Camp, J. Pécaut, C.E. Kefalidis, L. Maron, S. Gambarelli, M. Mazzanti, J. Am. Chem. Soc. 136 (2014) 6716–6723.

18. (a) O.T. Summerscales, A.S. Frey, F.G.N. Cloke, P.B. Hitchcock, Chem. Commun. (2009) 198–200. (b) E.M. Matson, A.T. Breshears, J.J. Kiernicki, B.S. Newell, P.E. Fanwick, M.P. Shores , J.R. Walensky, S.C. Bart, Inorg. Chem. 53 (2014) 12977–12985.

19. W. Ding, W. Fang, Z. Chai, D. Wang, J. Chem. Theory Comput. 8 (2012) 3605–3617.

20. L. Castro, L. Maron, Chem. –Eur. J. 18 (2012) 6610–6615.

21. C.J. Inman, A.S.P. Frey, A.F.R. Kilpatrick, F.G.N. Cloke, S.M. Roe, Organometallics 36 (2017) 4539–4545.

22. J.M. Berg, R.H. Holm, Interscience vol. 4 (1982), New York.

23. D. Coucouvanis, Ace. Chem. Res. 24 (1991) 1–8.

24. B.C. Wiegand, C.M. Friend, Chem. Rev. 92 (1992) 491–496.

25. I. Santos, N. Marques, A. Pires de Matos, Inorg. Chim. Acta 139 (1987) 89–90.

26. Z. Lin, C.P. Brock, T.J. Marks, Inorg. Chim. Acta 141 (1988) 145–149.

27. K. Tatsumi, I. Matsubara, Y. Inoue, A. Nakamura, R.E. Cramer, G.J. Tagoshi, J.A. Golen, J.W. Gilje, Inorg. Chem. 29 (1990) 4928–4938.

28. (a) S.D. Stults, R.A. Andersen, A. Zalkin, Organometallics 9 (1990) 1623–1629. (b) A. Domingos, A. Pires de Matos, I. Santos, Polyhedron 11 (1992) 1601–1606.

29. D.L. Clark, M.M. Miller, J.G. Watkin, Inorg. Chem. 32 (1993) 772–774.

30. E.M. Matson, P.E. Fanwick, S.C. Bart, Organometallics 30 (2011) 5753–5762.

31. (a) P.C. Leverd, T. Arliguie, M. Lance, M. Nierlich, J. Vigner, M. Ephritikhine, J. Chem. Soc. Dalton Trans. (1994) 501–504. (b) P.C. Leverd, M. Ephritikhine, M. Lance, J. Vigner, M. Nierlich, J. Organomet. Chem. 507 (1996) 229–237.

32. C. Lescop, T. Arliguie, M. Lance, M. Nierlich, M. Ephritikhine, J. Organomet. Chem. 580 (1999) 137–144.

33. F.T. Edelmann, in: Wilkinson G, Stone FGA, Abel EW (Eds.) Comprehensive Organometallic Chemistry, vol. 4 (1995) Pergamon, Oxford, p. 11–130.

34. K.B. Wiberg, Tetrahedron 24 (1968) 1083–1096.

35. A.E. Reed, R.B. Weinstock, F. Weinhold, J. Chem. Phys. 83 (1985) 735–746.

36. Gaussian 09, Revision D.01, M.J. Frisch, G.W. Trucks, H.B. Schlegel, G.E. Scuseria, M.A. Robb, J.R. Cheeseman, G. Scalmani, V. Barone, B. Mennucci, G.A. Petersson, H. Nakatsuji, M. Caricato, X. Li, H.P. Hratchian, A.F. Izmaylov, J. Bloino, G. Zheng, J.L.

Sonnenberg, M. Hada, M. Ehara, K. Toyota, R. Fukuda, J. Hasegawa, M. Ishida, T. Nakajima, Y. Honda, O. Kitao, H. Nakai, T. Vreven, J.A. Montgomery, J.E. Peralta, F. Ogliaro, M. Bearpark, J.J. Heyd, E. Brothers, K.N. Kudin, V.N. Staroverov, R. Kobayashi, J. Normand, K. Raghavachari, A. Rendell, J.C. Burant, S.S. Iyengar, J. Tomasi, M. Cossi, N. Rega, J.M. Millam, M. Klene, J.E. Knox, J.B. Cross, V. Bakken, C. Adamo, J. Jaramillo, R. Gomperts, R.E. Stratmann, O. Yazyev, A.J. Austin, R. Cammi, C. Pomelli, J.W. Ochterski, R.L. Martin, K. Morokuma, V.G. Zakrzewski, G.A. Voth, P. Salvador, J.J. Dannenberg, S. Dapprich, A.D. Daniels, O. Farkas, J.B. Foresman, J.V. Ortiz, J. Cioslowski, D.J. Fox, Gaussian Inc. Wallingford CT, 2013.

37. A.D. Becke, J. Chem. Phys. 98 (1993) 5648–5652.

38. (a) J.P. Perdew, Y. Wang Phys. Rev. B 45 (1992) 13244–13249. (b) K. Burke, J.P. Perdew, W. Yang, (1998) in Electronic Density Functional Theory: Recent Progress and New Directions (Eds.: Dobson JF, Vignale G, Das MP), Springer, Heidelberg.

39. L. Castro, S.C. Bart, O.P. Lam, K. Meyer, L. Maron, Organometallics 29 (2010) 5504–5510.

40. (a) A. Moritz, M. Dolg Chem. Phys. 337 (2007) 48–54. (b) A. Moritz, X.Y. Cao, M. Dolg, Theor. Chem. Acc. 118 (2007) 845–854. (c) M. Dolg, H. Stoll, H. Preuss, J. Chem. Phys. 90 (1989) 1730–1734. (d) X. Cao, M. Dolg, J. Chem. Phys. 115 (2001) 7348–7355.

41. (a) M. Dolg, H. Stoll, A. Savin, H. Preuss, Theor. Chim. Acta 75 (1989) 173–194. (b) M. Dolg, H. Stoll, H. Preuss, Theor. Chim Acta 85 (1993) 441–450.

42. A. Bergner, M. Dolg, W. Kuechle, H. Stoll, H. Preuss, Mol. Phys. 80 (1993) 1431–1441.

43. A.W. Ehlers, M. Bohme, S. Dapprich, A. Gobbi, A. Hollwarth, V. Jonas, K.F. Kohler, R. Stegmann, A. Veldkamp, G.A. Frenking, Chem. Phys. Lett. 208 (1993) 111–114.

44. A.V. Marenich, C.J. Cramer, D.G. Truhlar, J. Phys. Chem. B 113 (2009) 6378-6396.

45. (a) W.J. Hehre, R. Ditchfield, J.A. Pople, J. Chem. Phys. 56 (1972) 2257–2261. (b) P.C. Hariharan, J.A. Pople, Theor. Chim. Acta 28 (1973) 213–222.

46. (a) L. Castro, A. Yahia, L. Maron, C. R. Chimie 13 (2010) 870–875. (b) L. Castro, A. Yahia, L. Maron, Chem. Phys. Chem. 11 (2010) 990–994.

47. V. Mougel, C. Camp, J. Pécaut, C. Copéret, L. Maron, C.E. Kefalidis, M. Mazzanti, Angew. Chem. Int. Ed. 51 (2012) 12280–12284.

48. S. Labouille, F. Nief, L. Maron, J. Phys. Chem. 115 (2011) 8295–8301.

49. L. Castro, C.E. Kefalidis, D. McKay, S. Essafi, L. Perrin, L. Maron, Dalton Trans. 43 (2014) 12124–12134.

50. L. Castro, S. Labouille, D.R. Kindra, J.W. Ziller, F. Nief, W.J. Evans, L. Maron, Chem. Eur. J. 18 (2012) 7886–7895.

51. (a) C. Gonzalez, H.B. Schlegel, J. Chem. Phys. 90 (1989) 2154–2161. (b) C. Gonzalez, H.B. Schlegel, J. Phys. Chem. 94 (1990) 5523–5527.

52. A.V. Marenich, C.J. Cramer, D.G. Truhlar, J. Phys. Chem. B 113 (2009) 6378–6396.

53. E. Van Lenthe, J.G. Snijders, E.J. Baerends, J. Chem. Phys. 105 (1996) 6505–6516.

54. H. Xiao, J. Li, Chin. J. Struct. Chem. 27 (2008) 967–974.

55. J.T. Lyon, L. Andews, P. Malmqvist, B.O. Roos, T. Yang, B.E. Bursten, Inorg. Chem. 46 (2007) 4917–4925.

56. L. Gagliardi, B.O. Roos, P. Malmqvist, J.M. Dyke, J. Phys. Chem. A 105 (2001) 10602–10606.

57. (a) R.S. Mulliken, J. Chem. Phys. 23 (1955) 1833–1840 and 2338–2342. (b) R.S. Mulliken, W.C. Ermler, (1977) Diatomic Molecules: Results of ab initio Calculations (Academic, New York) pp 33–38.

58. J. Marçalo, A. Pires De Matos, Polyhedron 8 (1989) 2431–2437.

59. A. Shaver, P.Y. Plouffe, P. Bird, E. Livingstone, Inorg. Chem. 29 (1990) 1826–1830.

60. A. Shaver, B.S. Lum, P. Bird, K. Arnold, Inorg. Chem. 28 (1989) 1900–1904.

61. M. Arroyo, S. Bernès, J. Cerón, J. Rius, H. Torrens, Inorg. Chem. 43 (2004) 986–992.